

Real-time observation of optical rogue waves in spatiotemporally mode-locked fiber lasers

Uğur Teğin ¹, Peng Wang¹ & Lihong V. Wang ¹✉

Fiber lasers offer tabletop nonlinear environments to mimic and study the complex dynamics of nature. Optical rogue waves, rarely occurring extreme intensity fluctuations, are one of the many subjects that can be investigated with a fiber laser cavity. Although oceanic rogue waves are a result of spatiotemporal dynamics, the single-mode nature of the fiber laser and the commonly used measurement techniques limit the optical rogue wave studies to only temporal dynamics. In this study, we overcome such limit to observe rogue wave real-time dynamics in spatiotemporally mode-locked fiber lasers by utilizing state-of-the-art compressed ultrafast photography technique. The multimode laser cavity exhibits long-tailed non-Gaussian distributions under relaxed cavity constraints. Single-shot spatiotemporal measurements of rogue events showed that, instead of noise bursts, the cavity produces clean pulses with high-quality beam profiles. Our results indicate that rogue events in spatiotemporally mode-locked fiber lasers undergo nonlinear spatial transformation due to a power-dependent consistent attractor.

¹Caltech Optical Imaging Laboratory, Andrew and Peggy Cherg Department of Medical Engineering, Department of Electrical Engineering, California Institute of Technology, 1200 E. California Blvd., MC 138-78, Pasadena, CA 91125, USA. ✉email: lvw@caltech.edu

Over the centuries, sailors have told tales of giant waves that appeared on high seas without warning, destroyed vessels, and disappeared without a trace. After first time recorded by a measurement instrument in 1995 at Draupner platform in the North Sea¹, these rarely occurring, rogue waves transitioned from being a part of sailors' lore to a topic of intense study of oceanography. In oceanography, rogue waves are defined as surface waves with a height exceeding eight times the standard deviation of the surface elevation which is equal to twice the significant wave height². In the following years, the concept of rogue waves has been extended and in addition to oceanic rogue waves, acoustic, thermal, and even financial rogue waves have been reported³. In 2007, high intensities with similar statistics are reported in the supercontinuum generation process, during a dramatic spectral broadening in optical fibers, with dispersive Fourier transform technique in real-time measurement⁴. These temporally rare intensity fluctuations are analogous to oceanic rogue waves. This discovery led to extensive studies of the impact of noise on seed pulse to supercontinuum generation and soliton dynamics in single-mode fibers^{5–8}. Besides temporal studies, rogue waves have also been investigated spatially using nonlinear systems like optical filamentation in gas⁹ and linear systems combining spatial inhomogeneity and highly multimode fibers as diffusing media¹⁰.

With the incorporation of gain, saturable absorbers, and other dissipation elements, the nonlinear transfer functions of single-mode fiber lasers are considered even more complex than that of single-pass nonlinear propagation in fibers. As a result, lasers with external injection, mode-locking, and delayed feedback can exhibit complex noise characteristics with spikes in output intensity. Mode-locked fiber lasers are classified by the net dispersion of their laser cavities, which determines the types of pulses they generate as a result of nonlinear laser dynamics. In theory, a laser cavity generates an identical pulse every roundtrip. In reality, fundamental mode-locked lasers are closest to this ideal laser cavity, and their output parameters follow Gaussian distributions¹¹. To create a highly chaotic environment, gain, loss, and/or saturable absorption parameters must be adjusted to divert the laser cavity from the equilibrium point. As a result of such adjustments, noise-like pulses can form¹², or multiple pulses can form per cavity through harmonic mode-locking¹³ or stimulated Raman scattering¹⁴. An anomalous dispersion cavity with a chaotic multi-pulse regime led to the first demonstration of rogue waves in fiber lasers, which had been predicted by numerical studies^{15,16}. Later, similar laser output behavior was observed in a normal dispersion cavity with a noise-like mode-locking regime¹⁷. In the following years, various laser operations were investigated and they were summarized in a recent review article¹⁸.

By exploiting relatively low modal dispersion and periodic self-imaging properties of graded-index multimode fibers (GRIN MMFs), the spatiotemporal mode-locking mechanism has been proposed with multimode fiber cavities¹⁹. With coherent superposition of transverse and longitudinal modes in a multimode laser cavity, fiber lasers can be powered up via spatiotemporal mode-locking. Following the initial demonstration of dissipative soliton pulses with spatiotemporally mode-locked fiber lasers, bound-state solitons²⁰ and harmonic mode-locking²¹ have been reported as well. In addition to all-fiber spatiotemporally mode-locked lasers with superior stability^{22,23}, self-similar pulse propagation is proposed to enhance beam quality²⁴. Complementing this mode-locking mechanism, a nonlinear beam cleaning effect presented as a result of a universal unstable attractor in GRIN MMFs with a single-pass orientation^{25–27}. This attractor initially causes a nonlinear spatial transformation to an arbitrary input field and results in a high-quality beam with a weak background of higher-order modes²⁸. Due to its unstable nature, with

increasing power, the attractor triggers spatiotemporal instability to propagating field and results in the formation of Stokes and anti-Stokes peaks with high-quality beam profiles^{29,30}. Spatiotemporally mode-locked fiber lasers inherit this attractor via the GRIN MMF sections of the cavity. However, the relatively short GRIN MMF lengths form a challenge to realize the nonlinear beam cleaning in a laser cavity and requires high powers to observe the effects of the attractor. Recently, by tailoring cavity dynamics with a dispersion-managed design, nonlinear beam cleaning a spatiotemporally mode-locked fiber laser reported and resulted in single-mode beam profile with >20 nJ pulse energy³¹. When compared to single-mode fiber lasers, with bringing spatial interactions to the mode-locking mechanism, spatiotemporally mode-locked lasers offer an ideal test bed to study the complex multimode nonlinear wave dynamics under partial feedback conditions. Using a genetic algorithm approach, an intracavity wavefront shaping technique was used to demonstrate active control over the nonlinear mode-locking mechanism³². Furthermore, with the compressed ultrafast photography (CUP) technique, real-time non-repeating dissipative soliton dynamics have been studied and the results demonstrated the rich dynamics of spatiotemporally mode-locked lasers³³.

Results and discussion

Here, we present optical rogue wave dynamics, to the best of our knowledge, for the first time in a spatiotemporally mode-locked fiber laser. We investigate real-time changes in laser output under relaxed saturable absorber conditions and observe rarely occurring pulses with intensities up to 13 times greater than the standard deviation of the laser's output. With our CUP unit, we study these rogue events' spatial and temporal properties. The beam profile and shape of pulses with rogue events show distinct changes both temporally and spatially. Furthermore, our CUP unit enables us to study the intrapulse evolution of pulses with intensities above and below the rogue wave threshold (RWT), 8σ. Our measurements indicate that the consistent attractor in the spatiotemporally mode-locked fiber laser shapes the spatial distribution of the rogue events. For a better understanding of the nonlinear spatiotemporal propagation of pulses in a laser cavity, numerical simulations were performed. The Kerr-induced nonlinear beam cleaning effect is also observed numerically for pulses with rogue event intensities propagating through the GRIN MMF section of the cavity. We demonstrate that rogue wave dynamics can be formed by the multimode nonlinear transfer function of the spatiotemporally mode-locked fiber lasers. We conclude that nonlinear beam cleaning is bound to occur for rogue events in spatiotemporally mode-locked lasers because the universal consistent attractor in GRIN MMFs is power-dependent.

Experimental studies. With the help of optical feedback, laser cavities can offer rich nonlinear dynamics while creating a balance between dispersion, amplification, and dissipation. This complex interaction gives rise to a nonlinear transfer function in a form of a quintic complex Ginzburg-Landau equation^{34–36}. In the presence of spatial coordinates and their corresponding terms (diffraction, refractive index, etc.), this nonlinear transfer function is modified to model spatiotemporally mode-locked fiber lasers as,

$$\frac{\partial U}{\partial z} = \frac{i}{2k_0} \nabla^2 U - \left(\sum_{n \geq 2} \beta_n \frac{\partial^n}{\partial T^n} \right) U + (\alpha + iy)|U|^2 U + \delta|U|^4 U - \frac{ik_0}{R^2} I(x, y)U + (g - l)U \quad (1)$$

where $U(x, y, z, T)$ is the slowly varying envelope of a multimode field oscillating inside the laser cavity, z is the propagation

direction, $k_0 = \omega_0 n_0 / c$ is the wave number where ω_0 is the center frequency and n_0 is the refractive index of the medium, ∇^2 describes the diffraction along the x and y as $\frac{\partial^2}{\partial x^2} + \frac{\partial^2}{\partial y^2}$, β_n denotes the higher order dispersion coefficients, T is the retarded time and defined as $T = t - z/v_g$ where v_g is the group-velocity of the pulse, α and δ are the cubic saturable and quintic absorption coefficients, γ is the cubic refractive nonlinearity coefficient of the fiber, R is the fiber core radius, $I(x, y)$ is the fiber refractive index profile, g and l are the wavelength-dependent net gain and loss terms of the cavity. Here, the fiber dependent variables such as β_n , γ , R and $I(x, y)$ change for each fiber section inside the laser cavity.

We anticipate this spatiotemporal nonlinear transfer function can transform small input fluctuations into extreme statistical variations yielding long-tailed statistics and rogue events. We studied the spatiotemporal changes in the output of a spatiotemporally mode-locked laser under relaxed saturable absorber conditions to investigate this possibility. While fundamental mode-locking creates highly stable output traces with strong saturable absorbers (see Supplementary Note 1), a relaxed saturable absorber creates unstable laser behavior in which optical noise bursts (noise-like pulses) form. By reducing the strength of the low-intensity suppression of the saturable absorber in our laser cavity, we can achieve such constraints. Such an unstable operation regime is suitable to investigate rogue events in spatiotemporally mode-locked lasers. The laser we developed for this study is shown in Fig. 1a. It is a dispersion-managed cavity with a positive net cavity dispersion ($\beta_{(2)net}$) of 8240 fs². We employed nonlinear polarization evolution (NPE) technique as the saturable absorber³⁷. Under relaxed saturable absorber configuration, the laser generates noise-like pulses with ~70 mW average power and around 22 MHz repetition rate (see Supplementary Note 2). The details of the laser cavity are described in Methods.

By using the CUP technique, we were able to study the pulse-to-pulse changes of the laser in real-time. CUP is a single-shot ultrafast imaging technique that can achieve an unprecedented maximum imaging speed of 70 trillion frames per second^{38,39}. In the CUP imaging module (see Fig. 1), the dynamic scene is first spatially encoded by a static pseudo-random binary pattern, displayed by a digital micromirror device (DMD). The encoded scene is then relayed to a streak camera whose entrance aperture is wide open to collect the entire two-dimensional x - y images. The streak camera temporally shears the ultrafast scene in the y -direction and acquires a single temporally integrated raw image. A regularization-based algorithm is then adopted to accurately recover the ultrafast image sequence from this highly compressed raw image^{40,41}. CUP's imaging speed is primarily determined by the selected shearing speed (i.e. the time range setting) of the streak camera. Further details can be found in Supplementary Note 3. It is significant to note that we can switch to different imaging modes by using different types of DMD patterns for our investigation of rogue dynamics in the spatiotemporally mode-locked fiber laser.

First, we investigated the temporal intensity changes between the output pulses. For this purpose, by applying a plane mask to the DMD of our CUP unit, we utilized the direct streak camera imaging without needing image reconstruction. By setting the time range to 400 ns, we captured 8 pulses per measurement. After 300 consecutive measurements we acquired a large set of pulses. To establish a time trace, we digitally selected the cross-sections which pass through the centers of pulses from these measurements. The time trace which represents the temporal intensity fluctuations in these 300 measurements (containing ~2400 pulses) is presented in Fig. 1b. To simplify the representation, we normalized the intensity measurements with the standard deviation of intensity of the time trace (σ). Pulses with intensities beyond RWT are rarely detected. To characterize

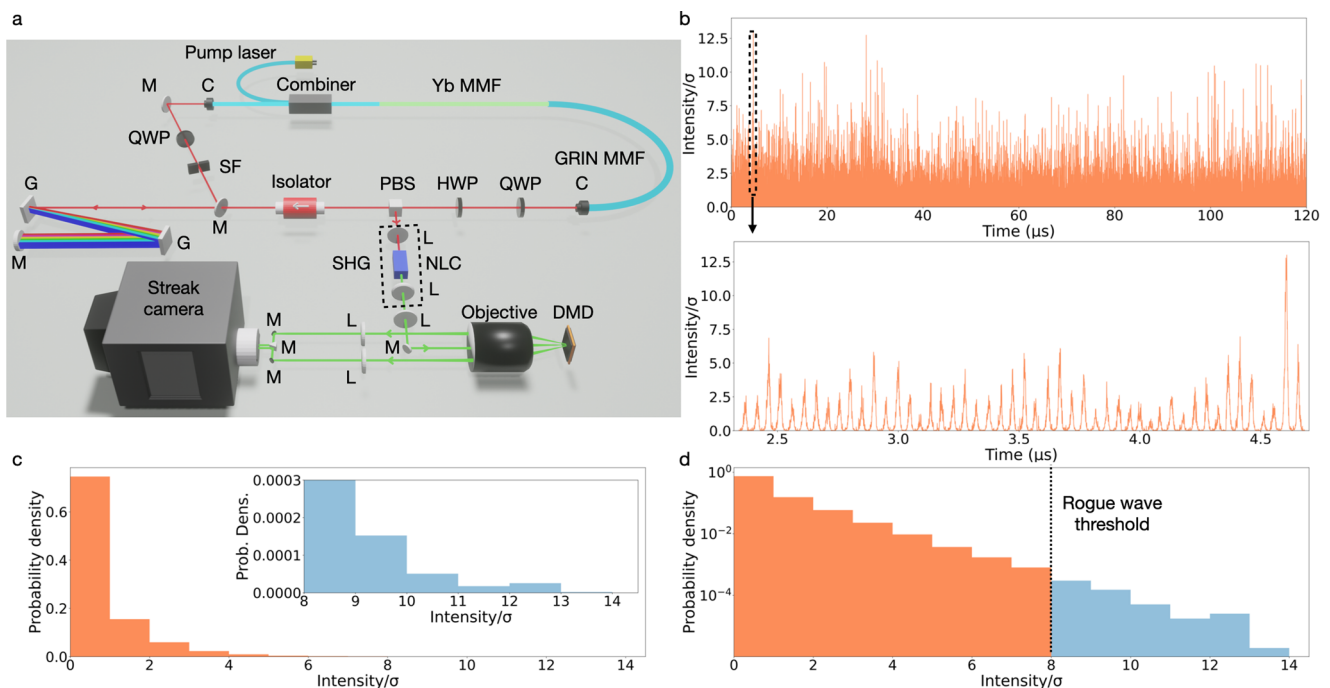


Fig. 1 Experimental setup and temporal measurements. **a** Schematic of the setup including the laser cavity, second-harmonic generation, and CUP units. Yb MMF Ytterbium-doped multimode fiber, GRIN MMF graded-index multimode fiber, C collimator, G diffraction grating, QWP quarter-wave plate, HWP half-wave plate, PBS polarizing beamsplitter, M mirror, SF spatial filter, L lens, SHG second-harmonic generation, NLC nonlinear crystal, DMD digital micromirror device. **b** Temporal intensity profile normalized to the standard deviation of intensity of the time trace (σ). **c** Histogram of the temporal intensity profile shown as normalized probability density. **d** The same histogram on semi-logarithmic axis.

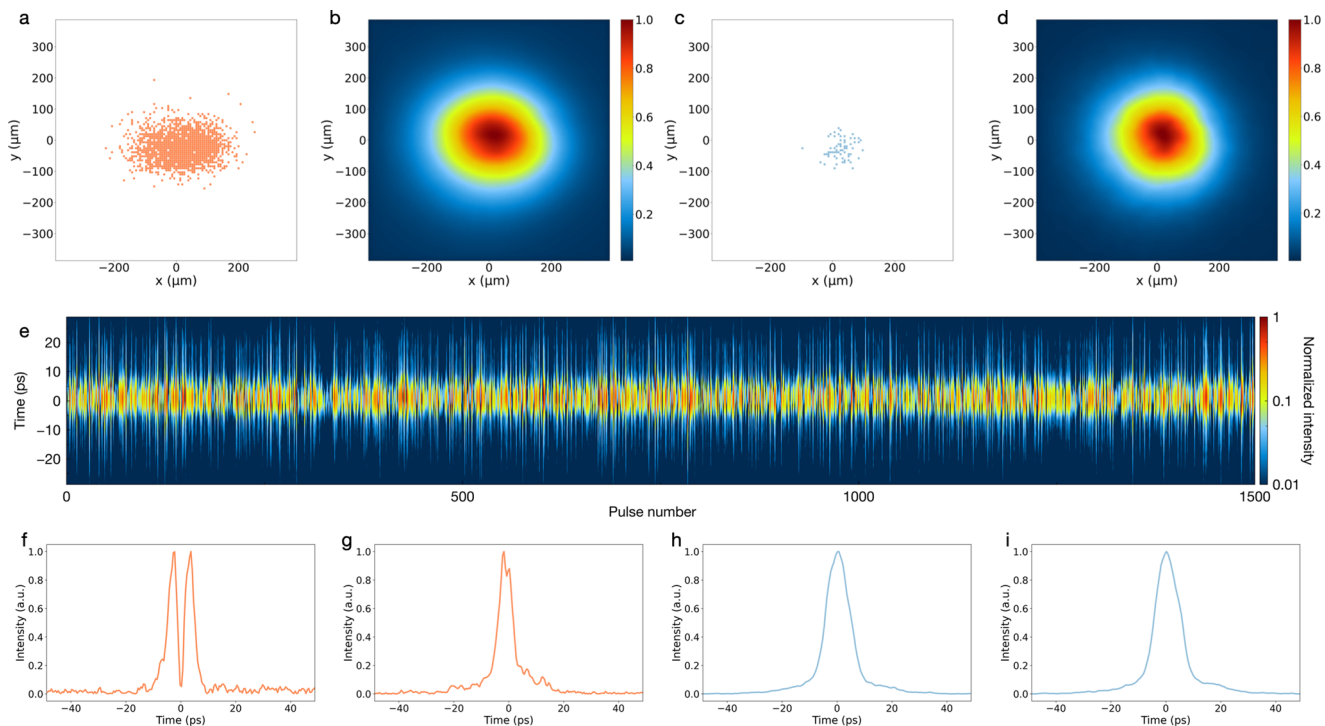


Fig. 2 Spatial and temporal measurements. **a** Position of the maximum intensity for each pulse in the dataset containing streak camera images. **b** Average beam profile calculated from all the pulses in the dataset. **c** Position of the maximum intensity for each pulse with rogue event. **d** Average beam profile calculated from the pulses with rogue events. **e** Stack of 1500 noise-like pulse shapes presented with a logarithmic intensity scale (normalized to maximum of the dataset). **f, g** Normalized example temporal shapes of the pulses with intensities less than the rogue wave threshold. **h, i** Normalized example temporal shapes of the pulses with rogue events.

the statistics of these results, we computed an intensity histogram from the presented time series. In Fig. 1c, d, the intensity histograms represent the normalized temporal intensity profile in Fig. 1b on linear and semi-logarithmic axes, respectively. It is clear from Fig. 1c that the histogram (i.e. probability density) follows an L-shaped distribution. This long-tailed distribution is characteristic of rogue waves since high intensities rarely occur with a small probability. The inset of Fig. 1c presents the portion of the histogram where intensities are above the RWT. As expected, the probabilities of generating rogue events are highly rare and our results indicate that from 8σ threshold to 13σ is less than 0.0003. Figure 1d shows the same histogram with a semi-logarithmic axis and the RWT is shown as a dashed line.

Our next step is to analyze the streak camera images to study the spatial properties of these noise-like pulses. Figure 2a shows the position of the maximum intensity for each pulse in the dataset. Due to multimode nature of the laser cavity, spatial positions of the maximum intensities of noise-like pulses are highly dispersed. From the streak camera images, we calculated an average beam profile which exhibits a large and asymmetric intensity distribution, as shown in Fig. 2b. When the pulses with rogue event intensities are isolated, we observed that the maximum intensities of these pulses are positioned tightly around the center of the beam, as shown in Fig. 2c. Similarly, a beam profile was also calculated for pulses with rogue events (see Fig. 2d). By fitting 2D Gaussian distributions to each of the beam profiles, we were able to compare them quantitatively. The average beam profile of the noise-like pulses (Fig. 2b) has a full width at half maximum (FWHM) of $164\ \mu\text{m}$ along the x-axis and $191\ \mu\text{m}$ along the y-axis, and this yields a ratio of 0.86. On the other hand, the average beam profile of the pulses with rogue events (Fig. 2d) has an FWHM of $156\ \mu\text{m}$ along the x-axis and $164\ \mu\text{m}$ along the y-axis this yields a ratio of 0.95.

To obtain individual pulse shapes, we changed the DMD pattern of our CUP unit to a slit mask and recorded the imaging setup's temporal impulse response. By setting the time range of CUP unit to 1 ns, we obtained sheared single pulse measurements. First, we measured the response of our CUP unit to slit DMD mask. By deconvolving the impulse response of the imaging system, we acquired individual pulse shapes from a set of streak camera images. A stack of 1500 noise-like pulse shapes is presented in Fig. 2e with a logarithmic intensity scale to illustrate the differences in both the pulse shapes and durations. We observed that the pulses with intensities below the RWT feature jagged burst-like pulse shapes (see the examples in Fig. 2f, g). On the other hand, the pulses with intensities above the RWT feature a well-structured pulse shape with a small pedestal background (see the examples in Fig. 2h, i). The pulse durations (FWHM) of these pulses vary between 7 ps and 14 ps.

Finally, we set the DMD pattern of our CUP unit to a pseudorandom binary pattern to record spatiotemporal intrapulse dynamics of our spatiotemporally mode-locked laser. The detail of the CUP operation is described in Methods. Similar to our previous measurements, we recorded 1500 pulses with 1 ns time range and achieved 2 Tfps frame rate. Later, we identified the pulses with rogue events from CUP images and performed image reconstruction to acquire spatiotemporal information per pulse. Figure 3 presents spatiotemporal changes of two example pulses with rogue events. To illustrate evolution of the pulses over spatiotemporal grid, at each temporal point we calculated a contour from the beam profiles by applying a threshold of 0.25 to intensity normalized 3D pulse distributions. These calculated contours are stacked over to demonstrate spatiotemporal shapes of the pulses. Furthermore, two example noise-like pulses with intensities below RWT are shown in Fig. 4. Similar to average beam profiles calculated directly from streak camera images

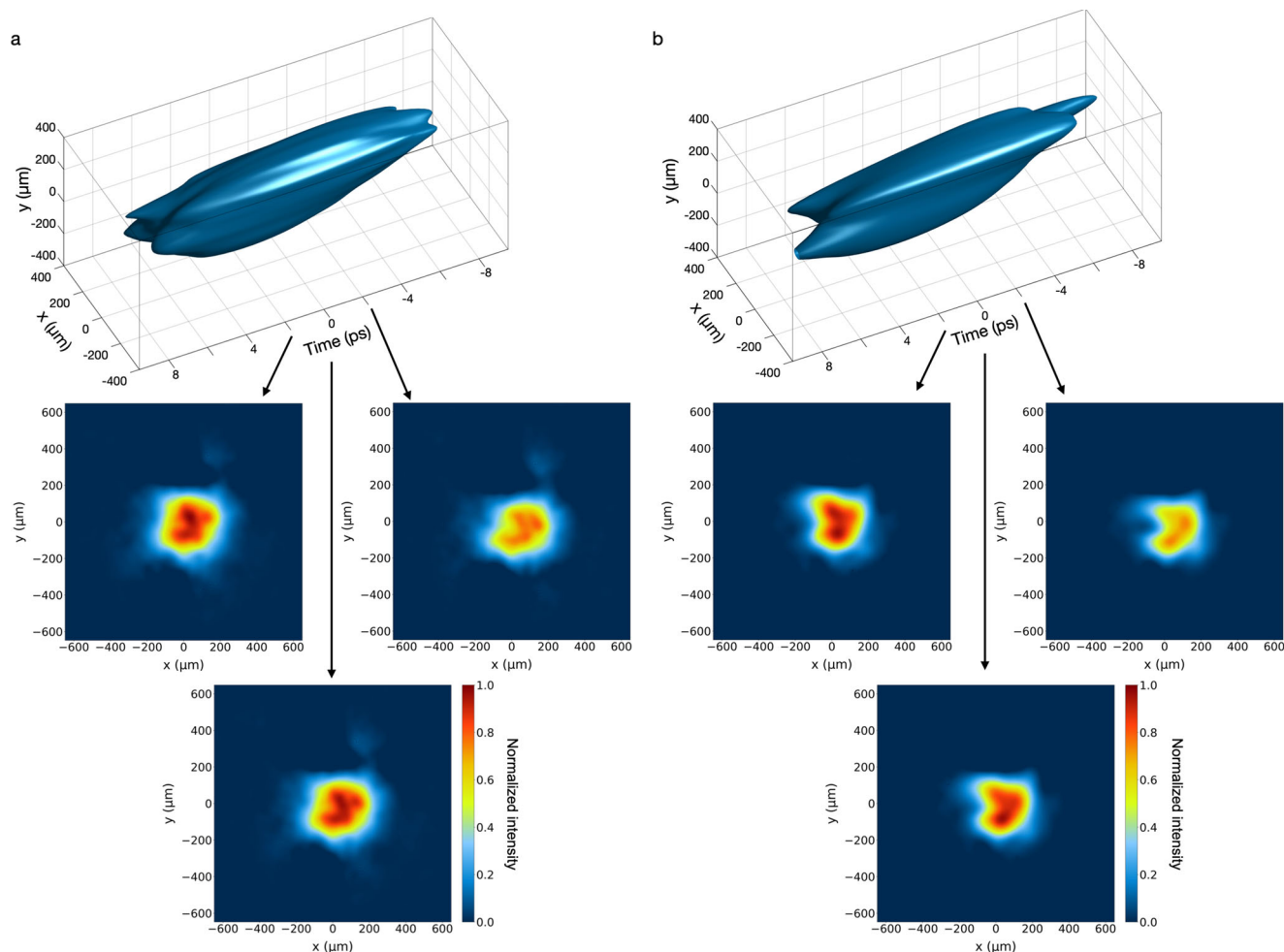


Fig. 3 Spatiotemporal distributions of example pulses with rogue events. a, b Reconstructed spatiotemporal intensity distributions of two example pulses with rogue events. These plots are achieved by calculating a contour from the beam profiles at each temporal point. Spatial distributions around the peaks of the pulses are presented separately by normalizing to local maxima and are shown in insets connected to the main panel by arrows.

(Fig. 2b, d), spatiotemporal measurements confirm that pulses with rogue events feature enhanced beam qualities. Spatiotemporal evolutions of these rogue and noise-like pulses are demonstrated in Supplementary Movies 1–4.

Numerical studies. We performed simulations with the time dependent beam propagation method^{42,43} to understand the effect of pulse power to spatial distribution of the pulse. Since the output beam profile of the fiber laser is heavily dependent on the GRIN MMF section, which is the last section before the NPE output of the laser, we studied the pulse propagating in this parabolic-index fiber. The simulation parameters are explained in detail in Methods.

For the same initial excitation condition and pulse, the effect of the pulse energy on the beam profile is presented in Fig. 5. From the experimental results, we measured the average power and the repetition rate of the laser and calculated the pulse energy of 3.2 nJ and denoted it with μ as the average pulse energy. For pulses with spatial distribution illustrated in Fig. 5 as the launched beam profile and energies of 1 μ , 8 μ , and 13 μ , we simulated the spatiotemporal nonlinear propagation inside the GRIN MMF and presented the beam profiles after 0.5 m, 1 m, 1.5 m, and 2 m (see Fig. 5a–c) where the fiber core is highlighted with the solid circles. The nonlinear beam cleaning effect can be observed by comparing the beam profiles after 2 m nonlinear propagation. The resulting spatial distributions are more confined and

symmetrical. As we report in Supplementary Note 4, we observed this beam quality improvement under a variety of launched beam profile conditions.

Conclusion

Unlike the conventional rogue wave studies with nonlinear fiber optics, this study provides an approach to investigate both spatial and temporal dynamics of rogue waves with a spatiotemporal nonlinear transfer function. Resorting to such an approach allows to draw several conclusions on the real-time dynamics of rogue waves. First of all, we observed that the resulting pulses from rogue events in a noise-like mode-locking regime are different from similar studies with single-mode lasers. In spatiotemporally mode-locked lasers, rogue events produce clean pulse shapes instead of high-intensity noise spikes¹¹.

Moreover, by resolving pulse to pulse changes, we investigated which long-tailed probability distribution best fits our observations of rogue events in a spatiotemporally mode-locked laser cavity. We observed that both intensity and pulse energy changes fit the Weibull distribution better than the Rayleigh distribution (see Supplementary Figs. 6 and 7). For the histograms calculated from the intensity changes and pulse energy changes, the Weibull distributions with parameters $\alpha = 0.536$ and $\beta = 0.72$ and $\alpha = 2.07$ and $\beta = 1.957$ provided better fits to the observed data.

The spatiotemporally mode-locked lasers overcome modal dispersion by using highly multimode GRIN MMFs and

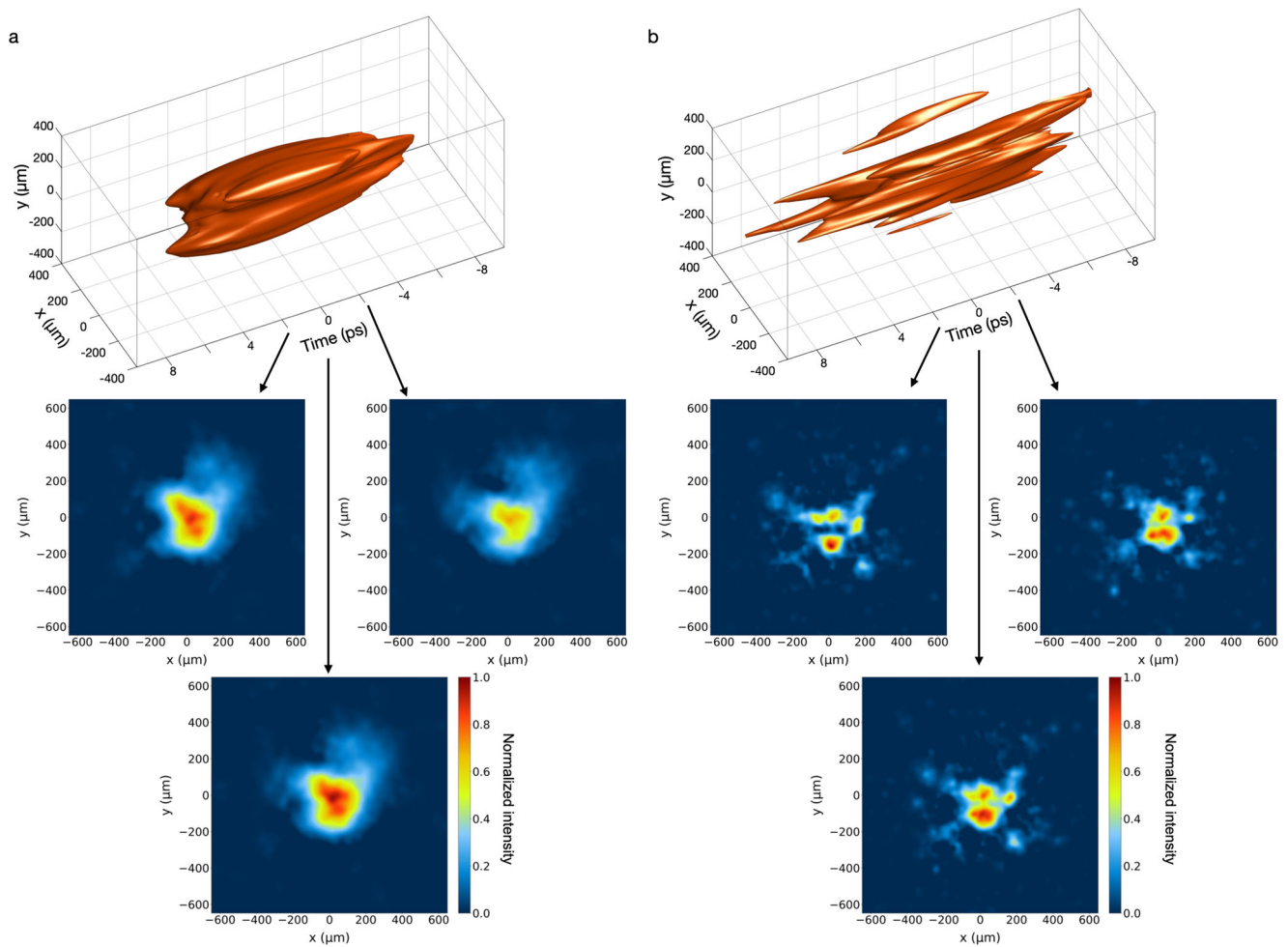


Fig. 4 Spatiotemporal distributions of example pulses with intensities lower than rogue wave threshold. **a, b** Reconstructed spatiotemporal intensity distributions of two example pulses with intensities lower than rogue wave threshold. These plots are achieved by calculating a contour from the beam profiles at each temporal point. Spatial distributions around the peaks of the pulses are presented separately by normalizing to local maxima and are shown in insets connected to the main panel by arrows.

few-mode step-index fibers. Thus, these fiber lasers inherit an unstable yet consistent attractor that introduces power-dependent nonlinear beam cleaning processes. Our results demonstrate that rogue events in multimode mode-locked fiber lasers are prone to be affected by this consistent attractor. Based on our experimental and numerical studies, we expect that rogue events in spatially mode-locked lasers always experience this nonlinear transformation. If rogue events are intensified further, this process may lead to spatiotemporal instability, due to the unstable nature of this attractor. It is essential to note that such a scenario will again feature a high-quality beam profile for pulses of high intensities.

Finally, the results of this study are of great interest to studies of spatiotemporal nonlinear optics including mode-locked fiber lasers. Since the nonlinear beam propagation in GRIN MMFs is governed by the temporal evolution of the three-dimensional Gross-Pitaevskii equation which is heavily used to model Bose-Einstein condensates^{44,45}, our observations also pertain to condensed matter physics where rogue dynamics are a subject of interest as well^{46,47}.

Methods

Laser oscillator. The oscillator is a dispersion-managed spatiotemporally mode-locked fiber laser similar to the one reported here³¹. A Yb-doped multimode gain fiber with a core size of 10 μm and 4 m length, a GRIN multimode fiber with a core size of 50 μm and 2 m length and a passive multimode fiber of pump combiner with a core size of 10 μm and 1.3 m lengths make the fiber part of the cavity.

Multimode pulse propagation is encouraged by splicing Yb-doped multimode gain fibers to GRIN multimode fiber with an offset (15 μm) and by coiling the GRIN fiber with a 25 cm diameter. The light is collimated after it passes through the fiber sections, and then it travels through waveplates, beam splitters, isolators, grating pairs (600 lines/mm), and a spatial filter (randomly placed adjustable slit). The spatial filter's purpose is to restrict the spatial distribution of the intracavity beam to ensure long-term stability. NPE is implemented with wave plates and a polarizing beam splitter as an artificial saturable absorber. To eliminate parasitic back reflections, GRIN fiber and step-index passive fiber are angle-cleaved on their free-space ends. Intracavity wave plates were adjusted to allow self-starting mode-locking conditions. A nonlinear crystal (uncoated Potassium Titanyl Phosphate with 9 \times 9 \times 7 mm dimensions and orientation angles of $\Theta = 90^\circ$ and $\varphi = 23.4^\circ$) is used as a frequency doubler since the CUP unit has an optimal sensitivity in visible wavelengths due to its photocathode within the streak tube.

Spatiotemporal simulations. To simulate fast nonlinear pulse propagation in the fiber, we implemented time-dependent beam propagation in Python.

$$\frac{\partial U}{\partial z} = \frac{i}{2k_0} \left(\frac{\partial^2 U}{\partial x^2} + \frac{\partial^2 U}{\partial y^2} \right) - i \frac{\beta_2}{2} \frac{\partial^2 U}{\partial T^2} + \frac{\beta_3}{6} \frac{\partial^3 U}{\partial T^3} - \frac{ik_0 \Delta (x^2 + y^2)}{R^2} U + i\gamma |U|^2 \quad (2)$$

where $U(x, y, z, T)$ is the slowly varying envelope of a multimode field propagating in GRIN MMF, inside the laser cavity, z is the propagation direction, T is the retarded time and defined as $T = t - z/v_g$ where v_g is the group-velocity of the pulse, Δ is the relative index difference between the center of the core and the cladding of the fiber, R is the fiber core radius and γ is the cubic refractive nonlinearity coefficient of the fiber. Unlike Eq. 1 which describes the overall laser dynamics, Eq. 2 only represents the nonlinear propagation in GRIN MMF.

In time-dependent beam propagation method simulations, heavy multidimensional fast Fourier-transform calculations require long computation times thus we utilized GPU-parallelization in our code. In our simulations we

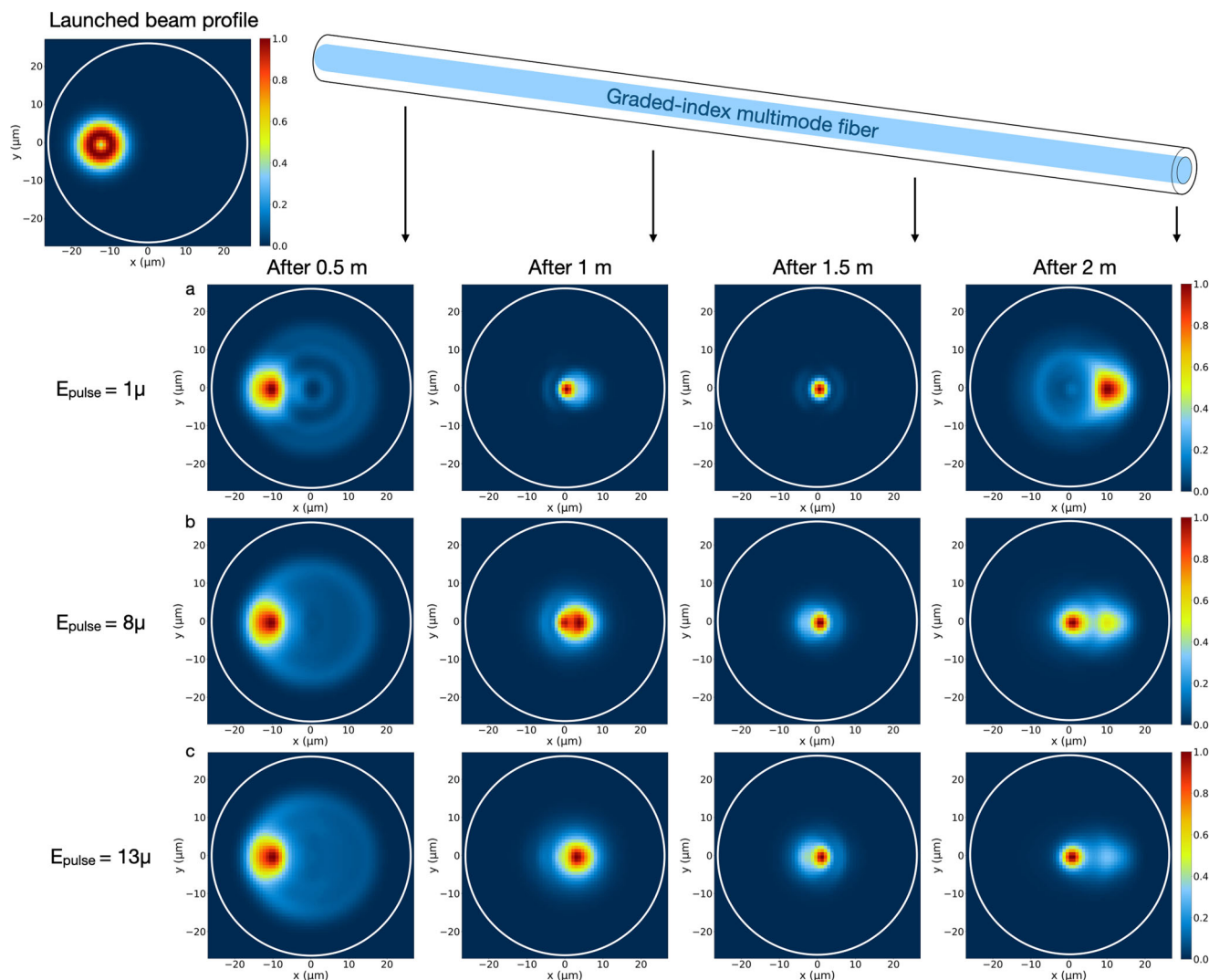


Fig. 5 Time-dependent beam propagation simulations inside the graded-index multimode fiber. **a** Spatial evolution of the pulse with the average pulse energy. **b** Spatial evolution of the pulse with eight times the average pulse energy. **c** Spatial evolution of the pulse with thirteen times the average pulse energy. Launched beam profile of the pulses is presented at top corner and solid circles indicate the core size of the GRIN MMF.

performed symmetrized split-step Fourier method to compute field propagation^{42,43}. In the simulation, pulses with a Gaussian temporal distribution centered at 1064 nm with an 8 ps duration (full-width at half-maximum) are numerically propagated for a fiber length of 2 m. The launched beam diameters ($1/e^2$) are set to Yb-doped gain fibers core size (10 μm) with 15 μm offset. The time window of the simulations is 100 ps with 61.5 fs temporal resolution and the spatial window is set as a 64×64 spatial grid with 0.84 μm spatial resolution. The numerical integration step is set to sample each self-imaging period ($\sim 555 \mu\text{m}$) 16 times to simulate GRIN MMF's spatial self-imaging correctly. We created an absorptive boundary condition around the core by truncating the parabolic fiber index profile with a super-Gaussian filter.

Data availability

The data that support the findings of this study are available from the corresponding author on reasonable request and in the Supplementary Information.

Supplementary Movies 1–4 contain further information on example rogue events and pulses with low intensities.

Code availability

The reconstruction algorithm is described in detail in Methods and Supplementary Information. We have opted not to make the computer code publicly available because the code is proprietary and used for other projects.

Received: 9 September 2022; Accepted: 21 March 2023;

Published online: 05 April 2023

References

- Sand, S. E., Hansen, N., Klinting, P., Gudmestad, O. T. & Sterndorff, M. J. Freak wave kinematics. in *Water wave kinematics* 535–549 (Springer, 1990).
- Müller, P., Garrett, C. & Osborne, A. Rogue waves. *Oceanography* **10**, 66 (2005).
- Ruban, V. et al. Rogue waves—towards a unifying concept? Discussions and debates. *Eur. Phys. J. Spec. Top.* **185**, 5–15 (2010).
- Solli, D. R., Ropers, C., Koonath, P. & Jalali, B. Optical rogue waves. *Nature* **450**, 1054–1057 (2007).
- Dudley, J. M., Dias, F., Erkintalo, M. & Genty, G. Instabilities, breathers and rogue waves in optics. *Nat. Photonics* **8**, 755–764 (2014).
- Akhmediev, N. et al. Roadmap on optical rogue waves and extreme events. *J. Opt.* **18**, 063001 (2016).
- Dudley, J. M., Genty, G., Mussot, A., Chabchoub, A. & Dias, F. Rogue waves and analogies in optics and oceanography. *Nat. Rev. Phys.* **1**, 675–689 (2019).
- Belić, M. R., Nikolić, S. N., Ashour, O. A. & Aleksić, N. B. On different aspects of the optical rogue waves nature. *Nonlinear Dyn.* **108**, 1655–1670 (2022).
- Birkholz, S. et al. Spatiotemporal rogue events in optical multiple filamentation. *Phys. Rev. Lett.* **111**, 243903 (2013).

10. Arecchi, F. T., Bortolozzo, U., Montina, A. & Residori, S. Granularity and inhomogeneity are the joint generators of optical rogue waves. *Phys. Rev. Lett.* **106**, 153901 (2011).
11. Liu, Z., Zhang, S. & Wise, F. W. Rogue waves in a normal-dispersion fiber laser. *Opt. Lett.* **40**, 1366 (2015).
12. Horowitz, M., Barad, Y. & Silberberg, Y. Noiselike pulses with a broadband spectrum generated from an erbium-doped fiber laser. *Opt. Lett.* **22**, 799 (1997).
13. Wu, C. & Dutta, N. K. High-repetition-rate optical pulse generation using a rational harmonic mode-locked fiber laser. *IEEE J. Quantum Electron.* **36**, 145–150 (2000).
14. Li, D. et al. Raman-scattering-assistant broadband noise-like pulse generation in all-normal-dispersion fiber lasers. *Opt. Express* **23**, 25889–25895 (2015).
15. Soto-Crespo, J. M., Grelu, P. & Akhmediev, N. Dissipative rogue waves: extreme pulses generated by passively mode-locked lasers. *Phys. Rev. E* **84**, 016604 (2011).
16. Lecaplain, C., Grelu, P., Soto-Crespo, J. M. & Akhmediev, N. Dissipative rogue waves generated by chaotic pulse bunching in a mode-locked laser. *Phys. Rev. Lett.* **108**, 233901 (2012).
17. Lecaplain, C. & Grelu, P. Rogue waves among noiselike-pulse laser emission: an experimental investigation. *Phys. Rev. A* **90**, 013805 (2014).
18. Song, Y., Wang, Z., Wang, C., Panajotov, K. & Zhang, H. Recent progress on optical rogue waves in fiber lasers: status, challenges, and perspectives. *Adv. Photonics* **2**, 1 (2020).
19. Wright, L. G., Christodoulides, D. N. & Wise, F. W. Spatiotemporal mode-locking in multimode fiber lasers. *Science* **358**, 94–97 (2017).
20. Qin, H., Xiao, X., Wang, P. & Yang, C. Observation of soliton molecules in a spatiotemporal mode-locked multimode fiber laser. *Opt. Lett.* **43**, 1982 (2018).
21. Ding, Y., Xiao, X., Wang, P. & Yang, C. Multiple-soliton in spatiotemporal mode-locked multimode fiber lasers. *Opt. Express* **27**, 11435 (2019).
22. Wu, H. et al. Pulses with switchable wavelengths and hysteresis in an all-fiber spatio-temporal mode-locked laser. *Appl. Phys. Express* **13**, 022008 (2020).
23. Teğın, U., Rahmani, B., Kakkava, E., Psaltis, D. & Moser, C. All-fiber spatiotemporally mode-locked laser with multimode fiber-based filtering. *Opt. Express* **28**, 23433 (2020).
24. Teğın, U., Kakkava, E., Rahmani, B., Psaltis, D. & Moser, C. Spatiotemporal self-similar fiber laser. *Optica* **6**, 1412 (2019).
25. Krupa, K. et al. Spatial beam self-cleaning in multimode fibres. *Nat. Photonics* **11**, 237–241 (2017).
26. Liu, Z., Wright, L. G., Christodoulides, D. N. & Wise, F. W. Kerr self-cleaning of femtosecond-pulsed beams in graded-index multimode fiber. *Opt. Lett.* **41**, 3675 (2016).
27. Deliancourt, E. et al. Kerr beam self-cleaning on the LP₁₁ mode in graded-index multimode fibers. *OSA Contin.* **2**, 1089 (2019).
28. Wright, L. G. et al. Self-organized instability in graded-index multimode fibers. *Nat. Photonics* **10**, 771–776 (2016).
29. Krupa, K. et al. Observation of geometric parametric instability induced by the periodic spatial self-imaging of multimode waves. *Phys. Rev. Lett.* **116**, 183901 (2016).
30. Teğın, U. & Ortac, B. Spatiotemporal instability of femtosecond pulses in graded-index multimode fibers. *IEEE Photonics Technol. Lett.* **29**, 2195–2198 (2017).
31. Teğın, U., Rahmani, B., Kakkava, E., Psaltis, D. & Moser, C. Single-mode output by controlling the spatiotemporal nonlinearities in mode-locked femtosecond multimode fiber lasers. *Adv. Photonics* **2**, 056005 (2020).
32. Wei, X., Jing, J. C., Shen, Y. & Wang, L. V. Harnessing a multi-dimensional fibre laser using genetic wavefront shaping. *Light Sci. Appl.* **9**, 149 (2020).
33. Jing, J. C., Wei, X. & Wang, L. V. Spatio-temporal-spectral imaging of non-repeatable dissipative soliton dynamics. *Nat. Commun.* **11**, 2059 (2020).
34. Haus, H. A., Fujimoto, J. G. & Ippen, E. P. Structures for additive pulse mode locking. *J. Opt. Soc. Am. B* **8**, 2068 (1991).
35. Haus, H. A. Mode-locking of lasers. *IEEE J. Sel. Top. Quantum Electron.* **6**, 1173–1185 (2000).
36. Renninger, W. H., Chong, A. & Wise, F. W. Dissipative solitons in normal-dispersion fiber lasers. *Phys. Rev. A* **77**, 023814 (2008).
37. Hofer, M., Ober, M. H., Haberl, F. & Fermann, M. E. Characterization of ultrashort pulse formation in passively mode-locked fiber lasers. *IEEE J. Quantum Electron.* **28**, 720–728 (1992).
38. Gao, L., Liang, J., Li, C. & Wang, L. V. Single-shot compressed ultrafast photography at one hundred billion frames per second. *Nature* **516**, 74–77 (2014).
39. Wang, P., Liang, J. & Wang, L. V. Single-shot ultrafast imaging attaining 70 trillion frames per second. *Nat. Commun.* **11**, 2091 (2020).
40. Liang, J. et al. Single-shot real-time video recording of a photonic Mach cone induced by a scattered light pulse. *Sci. Adv.* **3**, e1601814 (2017).
41. Liang, J., Wang, P., Zhu, L. & Wang, L. V. Single-shot stereo-polarimetric compressed ultrafast photography for light-speed observation of high-dimensional optical transients with picosecond resolution. *Nat. Commun.* **11**, 5252 (2020).
42. Teğın, U., Dinç, N. U., Moser, C. & Psaltis, D. Reusability report: predicting spatiotemporal nonlinear dynamics in multimode fibre optics with a recurrent neural network. *Nat. Mach. Intell.* **3**, 387–391 (2021).
43. Teğın, U., Yildırım, M., Oğuz, İ., Moser, C. & Psaltis, D. Scalable optical learning operator. *Nat. Comput. Sci.* **1**, 542–549 (2021).
44. Pitaevskii, L. P., Stringari, S. & Stringari, S. *Bose-einstein condensation*. (Oxford University Press, 2003).
45. Bao, W., Jaksch, D. & Markowich, P. A. Numerical solution of the Gross-Pitaevskii equation for Bose-Einstein condensation. *J. Comput. Phys.* **187**, 318–342 (2003).
46. Sun, W.-R. & Wang, L. Matter rogue waves for the three-component Gross-Pitaevskii equations in the spinor Bose-Einstein condensates. *Proc. R. Soc. Math. Phys. Eng. Sci.* **474**, 20170276 (2018).
47. Tan, Y., Bai, X. D. & Li, T. Super rogue waves: Collision of rogue waves in Bose-Einstein condensate. *Phys. Rev. E* **106**, 014208 (2022).

Acknowledgements

We thank Manxui Cui and Xin Tong for fruitful discussions. We received no specific funding for this work.

Author contributions

U.T. designed and conducted the experiments with the assistance of P.W. on ultrafast imaging techniques. L.V.W. supervised the project. All authors wrote and revised the manuscript.

Competing interests

The authors disclose the following patent applications: WO2016085571 A3 (L.V.W.), U.S. Provisional 62/298,552 (L.V.W.), and U.S. Provisional 62/904,442 (L.V.W. and P.W.). The other authors declare no competing financial interests.

Additional information

Supplementary information The online version contains supplementary material available at <https://doi.org/10.1038/s42005-023-01185-1>.

Correspondence and requests for materials should be addressed to Lihong V. Wang.

Peer review information *Communications Physics* thanks the anonymous reviewers for their contribution to the peer review of this work.

Reprints and permission information is available at <http://www.nature.com/reprints>

Publisher's note Springer Nature remains neutral with regard to jurisdictional claims in published maps and institutional affiliations.

 **Open Access** This article is licensed under a Creative Commons Attribution 4.0 International License, which permits use, sharing, adaptation, distribution and reproduction in any medium or format, as long as you give appropriate credit to the original author(s) and the source, provide a link to the Creative Commons license, and indicate if changes were made. The images or other third party material in this article are included in the article's Creative Commons license, unless indicated otherwise in a credit line to the material. If material is not included in the article's Creative Commons license and your intended use is not permitted by statutory regulation or exceeds the permitted use, you will need to obtain permission directly from the copyright holder. To view a copy of this license, visit <http://creativecommons.org/licenses/by/4.0/>.

© The Author(s) 2023